Planetary and Space Science 137 (2017) 40–51

Contents lists available at ScienceDirect

Planetary and Space Science

journal homepage: www.elsevier.com/locate/pss

Stellar winds and planetary bodies simulations: Magnetized obstacles in super-Alfvénic and sub-Alfvénic flows

Y. Vernisse[f,g,*], J.A. Riousset[e], U. Motschmann[a,d], K.-H. Glassmeier[b,c]

[a] Institute for Theoretical Physics, T.U. Braunschweig, Germany
[b] Institute for Geophysics and Extraterrestrial Physics, T.U. Braunschweig, Germany
[c] Max Planck Institute for Solar System Research, University of Göttingen, Germany
[d] Institute for Planetary Research, D.L.R. Berlin, Germany
[e] Embry Riddle Aeronautical University, Daytona Beach, FL, United States
[f] Institut de Recherche en Astrophysique et Planétologie, Toulouse, France
[g] Université Paul Sabatier, Toulouse, France

ARTICLE INFO

Keywords:
Hybrid simulation
Planetary dipole
Plasma interaction
Currents
Space physics

ABSTRACT

Most planetary bodies are moving in the solar wind, in a stellar wind, or in a plasma flow within the magnetosphere of a planet. The interaction of the body with the flowing plasma provides us with various interaction types, which mainly depend on the flow speed, the magnetization of the body, its conductivity, the presence of an ionosphere, and the size of the body. We establish two cornerstones representing highly magnetized obstacles embedded in a super-Alfvénic and sub-Alfvénic plasma. Those two cornerstones complete the two cornerstones defined in our previous study on inert obstacles in super-Alfvénic and sub-Alfvénic regimes. Tracking the transitions between these cornerstones enable better understanding of the feedback of the obstacle onto the plasma flow. Each interaction is studied by means of the hybrid model simulation code AIKEF. The results are summarized in three dimensional diagrams showing the current structures, which serve as a basis for our descriptions. We identify the major currents such as telluric, magnetosonic, Chapman–Ferraro, and bow-shock currents as the signatures of the particular state of development of the interaction region. We show that each type of interactions can be identified by studying the shape and the magnitude of its specific currents.

1. Introduction

Planetary objects possessing an internal magnetic moment are studied in the Solar System through Mercury, Earth, the giant planets and Ganymede. There have been numerous studies on the impact of the solar wind on magnetospheres induced by an intrinsic planetary magnetic moment (Kivelson and Bagenal, 2007, and references therein). These focus in particular on the effect of the solar wind velocity in terms of Alfvén Mach number (e.g. Roelof and Sibeck, 1993; Shue et al., 1997; Lavraud et al., 2013). The planets of the Solar System are standing most of the time in a super-Alfvénic solar wind with velocities from 300 to 1000 km/s (Marsch, 2006). Interactions of a sub-Alfvénic solar wind with a planetary obstacle are rare, and only occur during particular events, such as coronal mass ejections (Chané et al., 2012). However, moons embedded in the magnetosphere of their host planets are mostly subjected to a sub-Alfvénic inflowing plasma. Nonetheless, one moon, Ganymede – embedded in the magnetosphere of Jupiter – has been proven to have an intrinsic dipole field (Kivelson et al., 1996). Several studies focus on those two parameters – the Solar wind Alfvén Mach number and planetary intrinsic field – and their influences, e.g. on the magnetopause position (Case and Wild, 2013), the reconnection rate (Borovsky, 2008), or global and topological studies (Gombosi et al., 2000; Ridley, 2007; Tsyganenko and Andreeva, 2015). Analysis has been performed using a range of magnetizations as a main parameter, with the purpose of describing the evolution of the magnetosphere as a function of the internal dipole strength and the inflowing plasma Mach number. Omidi et al. (2002, 2004) and Simon et al. (2006a) conducted such studies for simulations of an asteroid using various magnetic moments, while Boesswetter et al. (2004, 2007, 2010) and Kallio et al. (2008) simulated the time evolution of the now extinct Martian intrinsic dipole. Such extrapolations of interaction types have been performed using different parameters, in order to evaluate the magnetic field of extrasolar planets (Durand-Manterola, 2009), their signatures on a host star (Saur et al., 2013), or their potential observation (Farrell et al., 1999; Zarka, 2006). Electric current signatures in the magnetosphere have been extensively investigated via both simulations and

* Corresponding author at: Institute for Theoretical Physics, T.U. Braunschweig, Germany.
E-mail address: yoann.vernisse@irap.omp.eu (Y. Vernisse).

http://dx.doi.org/10.1016/j.pss.2016.08.012
Received 10 March 2015; Received in revised form 20 June 2016; Accepted 2 August 2016
Available online 23 January 2017

observations (e.g. Siscoe et al., 2000; Liemohn et al., 2013). Describing the current system is a convenient way to attach the topology of magnetosphere to its fundamental processes (Mauk and Zanetti, 1987). Magnetospheric permanent current systems that have been listed are the ring, tail, Chapman–Ferraro, field aligned and ionospheric currents (Ganushkina et al., 2015, and references therein). In this paper, we analyze various current systems as a function of the upstream plasma Alfven Mach number, and planetary intrinsic magnetic moment. We base our study on the interpretation of the results from the hybrid model code AIKEF. This paper is a continuation of Vernisse et al. (2013). First we explain how we identify the current systems from the simulation results, then we will summarize those systems into schematics. Details of simulations results are provided in the auxiliary material, where all aspects pertaining to the interpretation are introduced in detail.

2. The AIKEF simulation code

2.1. Model description

Hybrid models are a good compromise in plasma simulation between needs in computational time and physical description. For our study we use a 3-D particles-in-cell simulation based on the hybrid model: AIKEF. This stands for Adaptive Ion Kinetic Electron Fluid and it is based on the work by Bagdonat and Motschmann (2002a). Subsequent improvement have been developed and described by Mueller et al. (2011). The hybrid model treats electrons as a fluid and ions as particles. Three assumptions are applied when deriving the hybrid model equations: (1) quasi-neutrality, (2) masslessness of electrons, and (3) negligibility of the displacement current. The motion of each ion is derived using the momentum equation dominated by Lorentz's force. The AIKEF code has already shown its sturdiness to reproduce observations data, through simulations of the Moon (Wiehle et al., 2011; Wang et al., 2011) with data from ARTEMIS, Mercury (Wang et al., 2010; Mueller et al., 2012) with data from Messenger, Rhea (Roussos et al., 2008; Simon et al., 2012), Enceladus (Kriegel et al., 2009, 2011), Tethys (Simon et al., 2009) and Titan (e.g. Mueller et al., 2010; Simon et al., 2006b) with data from the Cassini spacecraft. The numerical challenges and techniques pertinent to AIKEF have been discussed in Mueller et al. (2011).

2.2. Simulation parameters

In this paper the results are presented and discussed using normalized quantities. The normalizations of the relevant quantities related to this work are described in Table 1. The average number of particle in each cell is 100. Also, particles start to split and merge 8 cells away from the boundary of the refined area in order to avoid artificial gradient (Mueller, 2011). The fundamental quantities, B_0, n_0, q_0, and m_0, are taken equal to the upstream plasma magnetic field, number density, particle charge, and particle mass, respectively. The other normalization factors naturally follow from the normalization procedure and can be expressed as functions of the above quantities. An example for each quantity is given for Earth-like upstream solar wind parameters in the last column. The reader is invited to refer to this table to convert the normalized results with the appropriate upstream parameters. Other fixed plasma parameters in this paper are ion plasma beta at initialization $\beta_i = 0.5$; electron plasma beta $\beta_e = 0.5$; planetary radius $R_p = 20x_0$, where the ion inertial length x_0 is defined in Table 1; and the planetary resistivity $\eta_p = 200\eta_0$. The radius is chosen to correspond to a Lunar-sized obstacle considering the upstream plasma parameters around the Moon, while the resistivity is set with the purpose of having a quasi-dielectric obstacle, in consistency with our previous study (Vernisse et al., 2013). All but two parameters are fixed for every simulation. Our variables are listed in Table 2, which consist in: (1) the magnitude of the internal magnetic moment of the obstacle and (2) the upstream stellar wind velocity. The ratio between the upstream velocity and the magnetic moment is illustrated by the stand-off distance which is expressed by:

Table 1
Table of normalizations with a typical set of values at Earth. The terms m_p and e are the mass of the proton and the elementary charge, respectively. One should note that the expressions here are written without any simplifications. A common simplification is to consider: $m_0 = m_p$ and $q_0 = e$. In this paper, we consider that $B_0 = B_{up}$, $n_0 = n_{up}$, $q_0 = q_{up}$, and $m_0 = m_{up}$ (with B_{up}, n_{up}, q_{up}, and m_{up} being the upstream stellar wind magnetic field magnitude, number density, particle charge, and particle mass, respectively), i.e., the normalization is made using the upstream stellar wind parameters. The term $v_{A,0}$ stands for the Alfvén velocity.

Quantity	Variable	Normalization[a]	Example
Fundamental quantities			
Magnetic field	B	B_0	5.0 nT
Number density	n	n_0	5.0 cm^{-3}
Mass	m_α	m_0	$1.0m_p$
Charge	q_α	q_0	$1.0e$
Secondary quantities			
Time	t	$t_0 = m_0/(q_0B_0)$	2.1 s
Length	x	$x_0 = (m_0/(\mu_0 q_0^2 n_0))^{1/2}$	$1.0\cdot10^2$ km
Velocity	u	$u_0 = x_0/t_0 = B_0/(\mu_0\rho_0)^{1/2} = v_{A,0}$	48 km/s
Current density	j	$j_0 = q_0 n_0 v_{A,0}$	3.9 nA/M^2
Electric field	E	$E_0 = v_{A,0}B_0$	$2.4\cdot10^{-4}$ V/m
Resistivity	η	$\eta_0 = E_0/j_0$	$6.2\cdot10^3$ Ω m
Magnetic moment	M	$M_0 = 4\pi B_0 x_0^3/\mu_0$	$5.3\cdot10^{13}$ A m^2

[a] With appropriate definition when necessary.

Table 2
Simulation parameters for the runs presented in this paper. The magnetic moments, surface magnetic field magnitudes, and velocities are normalized using Table 1. The term B_{surf} refers to the magnitude of the planetary field at $(x = 1R_p, 0, 0)$, v_{up} is the upstream plasma velocity, and L_{SO} refers to the stand-off distance, which expression is detailed in Section 2 and given by Eq. (1). The name of each case gives the orientation ($+\hat{z}$) and magnitude of the magnetic moment of the obstacle, and the upstream velocity of the stellar wind.

Case name	M $[M_0]$	B_{surf} $[B_0]$	v_{up} $[v_{A,0}]$	L_{SO} $[R_p]$	Figures
Cornerstones					
$+80\text{E}3M_0\hat{z}\|8v_{A,0}$ (Mercury-Type)	$80\cdot10^3$	10	8	1.38	1,2
$+40\text{E}3M_0\hat{z}\|0.5v_{A,0}$ (Ganymede-Type)	$40\cdot10^3$	5	0.5	2.08	3
Transitions					
$+10\text{E}3{+}10\text{E}3M_0\hat{z}\|8v_{A,0}$	$10\cdot10^3$	1.25	8	0.69	4
$+5\text{E}3M_0\hat{z}\|2v_{A,0}$	$5\cdot10^3$	0.62	2	0.84	5
$+40\text{E}3M_0\hat{z}\|2v_{A,0}$	$40\cdot10^3$	5	2	1.68	6
$+5\text{E}3M_0\hat{z}\|1v_{A,0}$	$5\cdot10^3$	0.62	1	0.97	7a
$+40\text{E}3M_0\hat{z}\|1v_{A,0}$	$40\cdot10^3$	5	1	1.94	7b

$$L_{SO} = \left(\frac{4B_{surf}^2}{B_{up}^2 + 0.88\mu_0 m_{up} n_{up} v_{up}^2}\right)^{1/6}, \tag{1}$$

with B_{surf} being the magnetic field magnitude from the planetary magnetic moment at ($x = 1R_p$, $y = 0$, $z = 0$). The terms B_{up}, m_{up}, n_{up} and v_{up} are the magnetic field, particle mass, number density, and the velocity of the stellar wind, respectively. In super-Alfvénic regimes, the dynamic pressure of the upstream plasma is higher than its magnetic pressure, but in sub-Alfvénic regime, the upstream magnetic field pressure is dominant. Since both regimes are treated in this paper, the upstream field term has been added in the stand-off distance equation (see details in Baumjohann and Treumann, 1996). The scenarios investigated in this work are listed in Table 2. They are identified by a name providing the normalized magnetic moment with its orientation and the upstream velocity in Alfvén Mach. Each set of parameters yields a set of surface field and stand-off distance given in the same table.

The magnetic moments treated in this paper range from $M = 100M_0$ to $M = 80{\cdot}10^3M_0$. These values can be compared to obstacles in the solar system. For example, at Mercury, measurements give $n_{\mathrm{up}} = 30\ \mathrm{cm}^{-3}$, $B_{\mathrm{up}} = 20$ nT for the upstream conditions, and the magnetic moment of Mercury is $M = 1.4{\cdot}10^{13}$ A m^2 (Mueller et al., 2012). These upstream parameters correspond to a normalized magnetic moment $M = 130{\cdot}10^3M_0$ (according to Table 1). Measurements at Ganymede give: $n_{\mathrm{up}} = 8\ \mathrm{cm}^{-3}$, $B_{\mathrm{up}} = 65$ nT, and the magnetic moment of Ganymede is $M = 4.8{\cdot}10^{15}$ A m^2 (Kivelson et al., 2004). These upstream parameters correspond to a normalized magnetic moment $M = 35{\cdot}10^3M_0$. Although the absolute magnetic moment of Ganymede is higher than the moment of Mercury, using normalized units shows that the interaction region is smaller at Ganymede than at Mercury, independent of the upstream velocity.

2.3. Simulation geometry

In this study, we present simulation results using a Southward ($-\hat{z}$) interplanetary magnetic field (IMF), and a northward planetary magnetic moment ($+\hat{z}$). Such a geometry is close to the typical northward interplanetary magnetic field that can be observed at Earth. Modeling of the magnetosphere under Northward IMF has been made earlier using models of "closed magnetosphere" (Piddington, 1979). However, it has been shown that in this configuration, reconnection occurs at the polar cusps, resulting in particle exchange between the solar wind and the magnetosphere (Fuselier et al., 2000; Lavraud et al., 2005). The upstream plasma is flowing in the $+\hat{x}$ direction (in contrary to GSE). Regarding the simulation grid configuration, for super-Alfvénic simulations, the simulation domain is $600x_0$ along the x-axis with 144 nodes, $300x_0$ along the y-axis with 96 nodes and $400x_0$ along the z-axis with 96 nodes. There are two more refinement of the grid close to the obstacle. The first level of refinement is a rectangle going from $-80x_0$ in front of the obstacle to the domain boundary downstream along the x-axis. Along the y- and z-axes, the refinement boxes is located from $-70x_0$ to $70x_0$. The second level of refinement is situated from $-60x_0$ along the x-axis to the boundary of the simulation domain. Along the y- and the z-axes, the second level of refinement extend from $-50x_0$ to $+50x_0$. The simulation domain used in sub-Alfvénic regime is $400x_0$ long along the x-axis, $300x_0$ along the y-axis, and $800x_0$ along the z-axis. We also use two level of refinement. The first level of refinement is a rectangle extending from $-80x_0$ to the downstream boundary along the x-axis. Along the y- and z-axes, the refinement box extends from $-50x_0$ to $+50x_0$. The second level of refinement extends from $-60x_0$ along the x-axis to the downstream simulation domain boundary, and from $-40x_0$ to $+40x_0$ along the y- and z-axes.

2.4. Currents

We distinguish the plasma structures by their current systems. A list of the currents encountered in the simulations realized for this paper is given in Table 3. The description of the structures via the currents let us show the configuration of the interaction region and the physical processes involved in one diagram (Mauk and Zanetti, 1987). Two types of currents can be distinguished: analytical currents and topological currents. We mean by analytical currents, currents that have an expression directly derived from Vlasov equation. These are mainly the diamagnetic current, the polarization current, the Pedersen current, and the field aligned current. Note that we do not discuss nor the Pedersen current in this paper, nor the field-aligned current, mostly triggered by ionospheric interactions and magnetosphere–ionosphere coupling, which are absent from the present study. Topological currents are currents related to the topology of the interaction region. In some case an expression can be derived for the whole current or part of it. The main topological currents discussed in this paper are the Alfvénic current, the Chapman–Ferraro (C–F) current, the bow-shock current, the magnetotail current, and the ring current. In addition to magnetospheric currents, we observed a telluric current, associated to the conductivity of the planet, which is simulated in our mode by a constant resistivity, provided in Section 2.

Table 3
Definitions of the currents encountered in the simulations presented in this paper. The first column provides the identification mark for each current in Figs. 1–7, while the second column gives its definition.

Current	Definition
j_{slow}	Due to slow magnetosonic wave related diamagnetic current
j_{fast}	Due to fast magnetosonic polarization current
j_{alf}	Alfvénic current
$j_{\mathrm{C-F}}$	Chapman–Ferraro current
j_{tel}	Telluric current
j_{bs}	Bow-shock current
j_{sho}	Shocklets current
j_{mtail}	Magnetotail current
$j_{\mathrm{mtail_2}}$	Secondary magnetotail current
j_{ring}	Ring current

The analytical currents are:

1. The diamagnetic current (noted in this paper j_{slow}) is linked to pressure gradient perpendicular to the magnetic field (Baumjohann and Treumann, 1996). A clear review and description of the fluid and particle view of the diamagnetic current has been made by Ganushkina et al. (2015).

2. The polarization current is linked to the Laplace force term in the Vlasov equation Baumjohann and Treumann (1996), such as, in a steady state:

$$u_i\nabla u_i = \frac{q}{m}(E + u_i \times B) + \frac{\nabla P}{mn} \tag{2}$$

We consider the term $E + u_i \times B$, which, multiplied by B/B^2 gives $E + u_i \times B = -u_{i,\perp} + u_E = -u_{pol}$ where $u_{i,\perp}$ is the bulk velocity perpendicular to the magnetic field, and u_E the $E \times B$ drift velocity. The term $u_{i,\perp} - u_E$ represents the local drift of the fluid, which in terms of currents becomes:

$$j_{pol} = -nq(E + u_i \times B) \times \frac{B}{B^2} \tag{3}$$

In this study, we will show that this current is attached to the propagation of magnetosonic fast waves as already illustrated in Vernisse et al. (2013) – and thus noted j_{fast} – where it has been shown to bound the fast mode wings of a Lunar type obstacle.

The topological currents investigated in this paper are:

1. The Alfvénic current noted j_{alf} in this paper is attached to Alfvénic perturbations of the magnetic field (no variation in the magnetic field magnitude and the density). In our study, it is mostly present around Alfvén wings, triggered by the obstacle and particularly developed at sub-Alfvénic regimes. Analytical analyses have been performed for this current but are restricted to ideal cases (Neubauer, 1998; Simon, 2015).

2. The Chapman–Ferraro (C–F) current marked $j_{\mathrm{C-F}}$ is attached to the compression of the planetary field on the dayside, and the draping of the planetary field on the night-side. The configuration of the C–F current is such as on the dayside, the C–F current cancels the planetary field away from the planet and increases the magnetic field in the magnetosphere. According to the geometry used in this paper, with a northward oriented planetary intrinsic magnetic moment, this leads to a dusk–dawn current in the equatorial plane and a dawn-dusk current at the polar cap.

3. The bow-shock current noted j_{bs} is linked to the bow-shock, and owing to our geometry (IMF directed southward), it is oriented from dusk to dawn. One should note that in our configuration, with a southward IMF and a northward planetary magnetic moment, the bow

shock current and the C–F currents are parallel in the equatorial plane.

4. The telluric current j_{tel} is a current linked to the conductivity of the planetary obstacle. In our code, the conductivity is given by the parameter *eta* in Section 2. The density of the telluric current is easily derived from the size of the obstacle, and the parameters of the solar wind (see Vernisse, 2014, for details).

5. The magnetotail current noted j_{mtail} in our study is attached to the extension of the magnetosphere downstream. Its configuration depends on the orientation of the planetary magnetic dipole, as it extends the field lines of the planetary intrinsic field in the lobes. In this paper, we will discuss a secondary magnetotail current (j_{mtail_2}), which is not attached to the planetary intrinsic field, but to the deformation of the solar wind downstream. This secondary magnetotail current is only pertaining to anti-parallel IMF and planetary magnetic moment.

6. The ring current j_{ring} is a current present inside the magnetosphere. It is a diamagnetic current linked to the peak in pressure inside the magnetosphere (Ganushkina et al., 2015). In order to observe a clear ring current, the ratio between the planetary moment and the upstream plasma pressure must be high enough so that a complete magnetosphere develops. This is not the case for most of the simulations presented in this paper.

A quick summary of each current present in this paper is provided in Table 3, with their respective denomination used in this paper. A color code is used in order to identify the currents on the figures. In the next section we will show how all this current appears among the various interaction regimes investigated in this paper. The discussion on the evolution of the above-mentioned current as a function of the planetary intrinsic field and the upstream plasma velocity will be made in the discussion section.

3. Results

3.1. Cornerstones in the parameter space

We define two cornerstones in the two-dimensional parameter space explored in this paper: (1) the case $+80\mathrm{E}3M_0\hat{\mathrm{z}}|8v_{\mathrm{A},0}$ (Mercury-Type) and (2) the case $+40\mathrm{E}3M_0\hat{\mathrm{z}}|0.5v_{\mathrm{A},0}$ (Ganymede-Type). The relevant parameters are provided in Table 2.

3.1.1. Planetary obstacle in super-Alfvénic regime: the Mercury-Type case

The major results of this paper are summarized in schematics based on the output from the numerical simulations. We first describe our way of investigation between simulation results and the final diagram for the case of the Mercury-Type ($+80\mathrm{E}3M_0\hat{\mathrm{z}}|8v_{\mathrm{A},0}$). Fig. 1 presents the simulation results for case $+80\mathrm{E}3M_0\hat{\mathrm{z}}|8v_{\mathrm{A},0}$. For this simulation, the upstream velocity is $v_{\mathrm{up}} = 8v_{\mathrm{A},0}$ (Alfvén Mach number 8), along $+\hat{\mathrm{x}}$, following the simulation geometry described earlier. Fig. 1a provides a front view of the interaction while Fig. 1b focuses on a tailside view. The surface magnetic field B_{surf} is stronger than the upstream field magnitude B_0 with $B_{\mathrm{surf}} = 10B_0$ and the stand-off distance in this case is $L_{\mathrm{SO}} = 1.38R_{\mathrm{p}}$. The $+80\mathrm{E}3M_0\hat{\mathrm{z}}|8v_{\mathrm{A},0}$ scenario presented here simulates a magnetized obstacle, which magnetic pressure at the surface is higher than the stellar wind dynamic pressure. In this situation, a bow-shock is formed ahead of the obstacle and the magnetopause is well defined. In the left panel, we identify a first current attached to the bow-shock and identified j_{bs} in both Figs. 1a and b. This current flows parallel to $\hat{\mathrm{y}}$ at the subsolar point (in the dusk–dawn direction), anti-sunward on the $\mathrm{y} > 0$-half space and sunward in the $\mathrm{y} < 0$-half space, consistent with the southward orientation of the IMF. A second current that we have annotated $j_{\mathrm{C-F}}$ is consistent with the compression of the planetary intrinsic field on the dayside. This current flows in the equatorial plane in the direction parallel to $\hat{\mathrm{y}}$ (in the dusk–dawn direction), i.e. parallel to the bow shock current j_{bs}. At the poles, $j_{\mathrm{C-F}}$ flows anti-parallel to $\hat{\mathrm{y}}$ (from dawn to dusk). This corresponds to a typical Chapman–Ferraro (C–F) current. A third current is noted j_{mtail}. This current flows in the nightside of the obstacle in the equatorial plane in the direction parallel to $\hat{\mathrm{y}}$. At the poles, j_{mtail} is also anti-parallel to $\hat{\mathrm{y}}$, thus parallel to the C–F current $j_{\mathrm{C-F}}$. This current is linked to the development of the intrinsic magnetic field of the obstacle in the lobes, with a positive B_x in the southern hemisphere, and a negative B_x in the northern hemisphere. This current flows in the equatorial plane through the typical neutral sheet which separates the two lobes of the magnetotail, and closes by the so-called theta-like configuration at the northern and southern magnetopause (Eastman et al., 1984). In the right Panel of Fig. 1, the previously described bow shock and C–F currents are annotated. The magnetotail current j_{mtail} is not represented, however, a secondary tail current is represented and identified j_{mtail_2}. In the equatorial plane, j_{mtail_2} flows anti-parallel to $\hat{\mathrm{y}}$, thus anti-parallel to j_{mtail}. In the northern and southern edges of the magnetosphere, the current j_{mtail_2} flows parallel to $\hat{\mathrm{y}}$. On the flanks, in the northern hemisphere, j_{mtail_2} flows anti-parallel to the magnetic field on the dusk side and parallel to the magnetic field on the dawn side. In the southern hemisphere, it flows parallel to the magnetic field on the dusk side and anti-parallel to the magnetic field on the dawn side. The configuration of this current is similar to the theta-like configuration of a typical magnetotail current. However, its direction is not determined by the planetary intrinsic dipole. We will discuss this current in detail in the appropriate discussion section. In the right Panel of Fig. 1, we also recognize a current noted j_{sho}. The current j_{sho} flows parallel to the equatorial plane in the form of singlets of currents following the curve of the bow-shock, and alternating duskward and dawnward directions. This current is obviously attached to the bow shock, and forms a post-shock wave, with multiple density jumps. Further investigation regarding this current is provided in the related discussion section. Such a current has been discussed by Bagdonat and Motschmann (2002b), using the denomination "shocklet current", we will thus reuse that denomination. The last current that we identify in this figure is the current denoted j_{fast}. The successive simulation results presented in this paper will show that this current is a polarization current related to the propagation of fast magnetosonic waves at the boundary of the nightside magnetopause, i.e. at the inner limit of the magnetosheath, and sometimes merges with the magnetotail current. The current j_{fast} flows sunward on the $\mathrm{y} > 0$-half space and anti-sunward on the $\mathrm{y} < 0$-half space.

The observations from the simulation output of the $+80\mathrm{E}3M_0\hat{\mathrm{z}}|8v_{\mathrm{A},0}$(Mercury-Type) interaction are gathered in the schematic provided as Fig. 2. The view shows the dayside plasma interaction region. Each current previously indicated are reproduced in the schematic. The purpose of such a schematic is to summarize our observations from the simulation in a much understandable form than the direct output of the simulation model. The simulation results on which are based those results are provided in the auxiliary material. Thus, we invite the reader to refer to the auxiliary material for the detailed results. One recalls that the upstream wind flows in the $+\hat{\mathrm{x}}$-direction, the planetary magnetic moment is along $\hat{\mathrm{z}}$ and the upstream field is along $-\hat{\mathrm{z}}$ (see Section 2). The directions of all the currents discussed as part of Fig. 1 are accurately reproduced in the diagram of Fig. 2. Specifically, the magnetopause related current such as the C–F current and the magnetotail current are plotted in orange, and noted $j_{\mathrm{C-F}}$ and j_{mtail}, respectively. The bow-shock current j_{bs} is represented in purple with squared arrows, while the shocklet current j_{sho} is displayed with gray arrows. The fast magnetosonic mode polarization current, noted j_{fast}, is represented in blue. Finally, the secondary magnetotail current j_{mtail_2} is drawn in red. Three semi-transparent layers are also displayed in the figure. The first one is covering the complete interaction area and is displayed in purple. It represents the bow-shock, and therefore is merged with the bow-shock current in our schematics. The orange semi-transparent layer on the dayside represents the dayside magnetopause, and is merged with the dayside Chapman–Ferraro current. The blue semi-transparent cone-like layer represents the outer boundary of the nightside magnetosphere. It is merged with the outer fast mode polarization current of the wake.

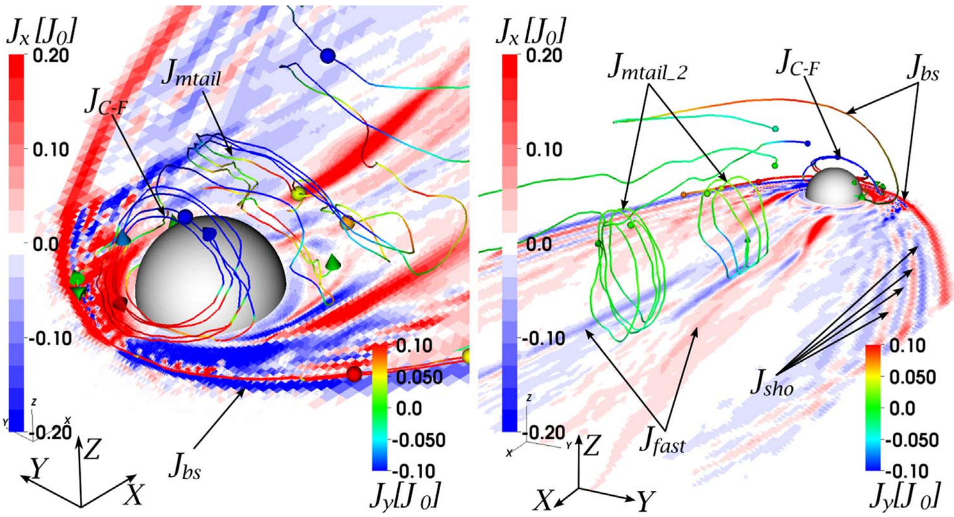

Fig. 1. x-Component of the current density in the equatorial plane for the front (a) and back (b) views of the $+80\text{E}3M_0\hat{z}|8v_{A,0}$ scenario, also called Mercury-Type. Blue areas are currents directed sunward and red areas are currents directed anti-sunward (left colorbar). The current density is normalized following Table 1. Current density streamlines are generated in several arbitrary points, and colored according to the value of their y-component (bottom right colorbar) to show the streamline directions. The parameters specific to each simulation type are given in Table 2. The description of each labeled current are provided in Table 3. (For interpretation of the references to color in this figure caption, the reader is referred to the web version of this paper.)

3.1.2. Planetary obstacle in sub-Alfvénic regime: the Ganymede-Type case

Most of the satellites in our Solar System orbit inside the magnetospheres of Jupiter and Saturn at sub-Alfvénic velocities (Kivelson et al., 2004). However, only Ganymede is known to possess an intrinsic magnetic field. At Ganymede, the planetary intrinsic dipole is pointing southward, opposite to the magnetic dipole of Jupiter, resulting in anti-parallel field configuration at the equivalent sub-solar point (e.g. Jia et al., 2009). This is different from the configuration that we investigate in this paper. Here the planetary field is pointing northward while the upstream field is pointing southward at sub-solar point. Thus, reconnection is expected to appear at the polar cap. The interpretations from our hybrid simulation are presented in Fig. 3. We use $v_{up} = 0.5v_{A,0}$ (Alfvén Mach number equals 0.5) as the upstream plasma speed. For the sake of concision, the simulation outputs are not presented in this section and only the schematic will be described. For further details concerning the simulation results, the reader is invited to refer to the auxiliary material. The simulation outputs of the $+40\text{E}3M_0\hat{z}|0.5v_{A,0}$ have been obtained using the methodology described in Section 3.1.1. Such an obstacle possesses a magnetic moment $M = 40{\cdot}10^3M_0$ leading to a surface magnetic field $B_{surf} = 5B_0$ and a stand-off distance $L_{SO} = 2.08R_p$ (see Table 2). As mentioned in Section 2, the upstream plasma flows along $+\hat{x}$, the planetary magnetic moment is directed along $\hat{z}$ while the upstream magnetic field is antiparallel to $\hat{z}$. The planetary magnetic field is confined inside the magnetopause – represented by the orange semi-transparent layer – bounded on the dayside by the C–F current j_{C-F} and on the nightside by the magnetotail current j_{mtail}, drawn in orange. The dayside component of the C–F current flows from dusk to dawn, in the equatorial plane, while the magnetotail current flows from dusk to dawn, consistent with typical C–F and tail current for such an intrinsic dipole field. We have noted in green a current flowing at the boundary of the void region generated by the deviation of the upstream particles by the magnetosphere of the obstacle. Such a void region is similar to the typical void found at the lunar wake (Whang, 1969), and bounded by a diamagnetic current,

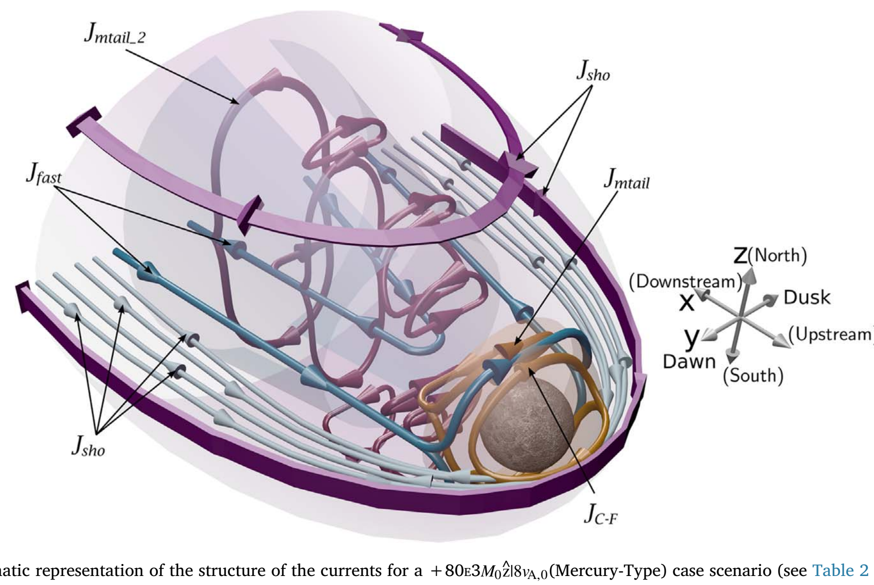

Fig. 2. Three dimensional schematic representation of the structure of the currents for a $+80\text{E}3M_0\hat{z}|8v_{A,0}$(Mercury-Type) case scenario (see Table 2 for parameters). The current j_{fast} is represented in blue, j_{mtail_2} in red, j_{sho} in cyan, j_{C-F} and j_{mtail} in orange, and j_{bs} in purple (see Table 3). The inner blue semi-transparent layer represents the nightside magnetopause, and the inner orange semi-transparent layer represents the dayside magnetopause. The outer purple semi-transparent layer represents the bow-shock. (For interpretation of the references to color in this figure caption, the reader is referred to the web version of this paper.)

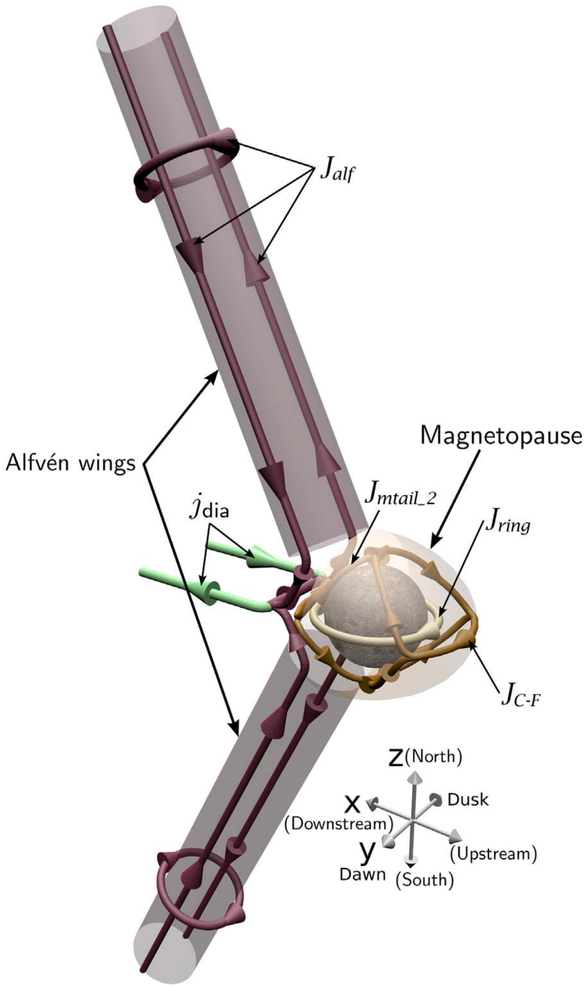

Fig.3. Three-dimensional diagram of the currents structures for a $+40\text{E}3M_0\hat{z}|0.5v_{A,0}$(Ganymede-Type) scenario (parameters in Table 2). Currents and obstacle details are the same as Fig. 2, except for magnetotail and Alfvenic currents, both represented in red. The stellar wind velocity is $v_{up} = 0.5v_{A,0}$. (For interpretation of the references to color in this figure caption, the reader is referred to the web version of this paper.)

generated by the density gradient between the void region and the surrounding plasma. Topologically, this current is attached to the propagation of slow magnetosonic waves triggered by the obstacle (Roussos et al., 2008). This system also triggers Alfvén wings, represented in Fig. 3 by semi-transparent red tubes attached to the magnetosphere. The Alfvénic current j_{alf} is represented by the red arrows flowing either parallel or perpendicular to the direction of propagation of the magnetic field, and thus, the Alfvén wings. This type of current is well known and has already been extensively described in the literature (for details see Neubauer, 1980; Saur et al., 1999; Simon et al., 2011; Simon, 2015). The last current that has been identified in our simulation results is noted j_{ring}. It flows clockwise when seen from above. The ring current at Earth flows clockwise and intensify the intrinsic field of the Earth (e.g. Haaland and Gjerloev, 2013, and references therein). The ring current represented in Fig. 3 flows in the opposite direction considering the orientation of the intrinsic field of the planetary obstacle. The reason why we call it a ring despite its non-conformity to the textbook ring current is because the simulation results show that it is a diamagnetic current. However the magnetosphere of our simulated obstacle is tenuous and the pressure gradient is directed outward of the obstacle. Details are provided in Section 4.

3.2. Intermediate situations between the cornerstones

In this section we investigate various obstacles under three different velocity regimes, namely the $+10\text{E}3M_0\hat{z}|8v_{A,0}$ scenario, with $v_{up} = 8v_{A,0}$, the $+5\text{E}3M_0\hat{z}|2v_{A,0}$ and $+40\text{E}3M_0\hat{z}|2v_{A,0}$ scenarios, with $v_{up} = 2v_{A,0}$, and the $+5\text{E}3M_0\hat{z}|1v_{A,0}$ and the $+40\text{E}3M_0\hat{z}|1v_{A,0}$, with $v_{up} = 1v_{A,0}$. We use the expression "weak dipole" to refer to planetary obstacles possessing a magnetic moment too weak to balance the upstream wind pressure, and therefore with a stand-off distance $L_{SO} < 1R_p$. The expression "strong dipole" refers to $L_{SO} > 1R_p$. The details on the stand-off distance derivation are provided in Section 2.

3.2.1. *From weak to strong magnetization: the $+10\text{E}3M_0\hat{z}|8v_{A,0}$ scenario*

The AIKEF simulation model is employed to study the transition regimes between the Lunar-Type and the Mercury-Type magnetizations. The most noticeable transition regime observed is presented in Fig. 4 and corresponds to the case $+10\text{E}3M_0\hat{z}|8v_{A,0}$ in Table 2. The magnetization of the obstacle in the $+10\text{E}3M_0\hat{z}|8v_{A,0}$ situation corresponds to a magnetic moment of $M = 10\cdot10^3M_0$, leading to a surface magnetic field $B_{surf} = 1.25B_0$ and a theoretical stand-off distance $L_{SO} = 0.69R_p$. We review the various currents observed in this particular simulation. On the dayside, three currents play a major role. First we recognize a current that flows from dusk to dawn in the equatorial plane, it is represented in yellow, and noted j_{tel}. This current is attached to the conductivity of the obstacle, and therefore called telluric current. When increasing the intrinsic moment of the planetary obstacle from 0

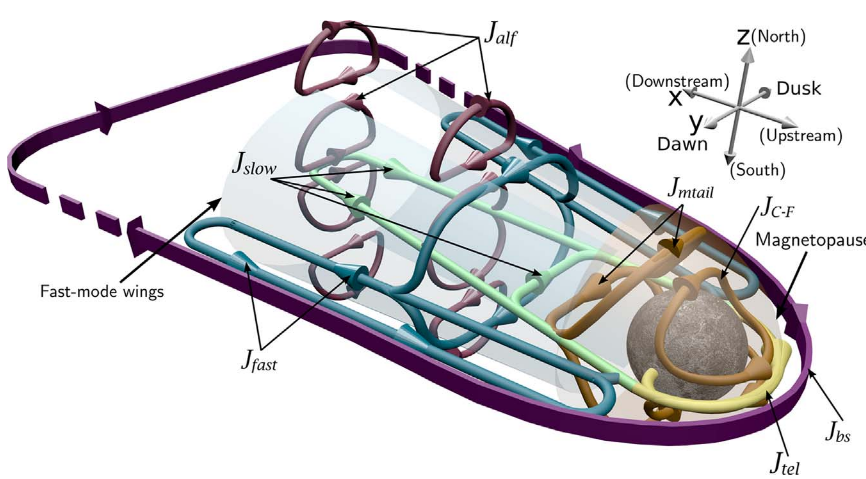

Fig. 4. Schematic representation in three-dimensions of the structure of the currents for the transition between Lunar-Type and Mercury-Type objects. This transition is called $+10\text{E}3M_0\hat{z}|8v_{A,0}$. Description of the currents is the same as in Fig. 3. The simulation parameters are given in Table 2. (For interpretation of the references to color in this figure caption, the reader is referred to the web version of this paper.)

to $10\cdot10^3 M_0$, this current remains present. Such currents related to the planetary conductivity have been investigated earlier at Mercury by Janhunen and Kallio (2004) and Jia et al. (2015). However, the telluric current studied here and by Janhunen and Kallio (2004) is a steady state current, unlike the induced current studied by Jia et al. (2015), which is triggered by the time variation of the upstream field (all simulation results presented in this paper are steady state solutions). Therefore, we adopt the term telluric current rather than induced current and describe its effect in the next section. A C–F current is recognizable in our simulation results on the dayside, and it is represented in the schematics of Fig. 4 in orange and noted $j_{\rm C-F}$. Its description is similar to the previously described C–F current in Fig. 2. The third current present on the dayside is the bow-shock current $j_{\rm bs}$, represented by purple squared arrows and which flows clockwise in the equatorial plane seen from above. In this regime of interaction, the bow-shock current is concentrated in a slab of $10x_0$ thickness centered on the equatorial plane (with e.g. $x_0 = 100$ km at Earth; see Table 1). A closing pattern of $j_{\rm bs}$ in the distant wake is represented via the dashed part of the current.

On the tailside of the interaction region, four currents are distinguishable in this regime of interaction. First, a diamagnetic current attached to the void existing behind the magnetosphere, $j_{\rm slow}$, is plotted in green. It is a slow mode current as introduced in the description of Fig. 3. More discussion concerning the development and disappearance of this current between the regimes of interaction will be brought in the successive description and summarized in the discussion section. One can note that a secondary diamagnetic current is also present in the center of the wake, flowing along $-\hat{y}$. This current has been introduced by Simon et al. (2012), and is linked to the pressure variation in the wake of the interaction region, in the direction of the flow. The magnetotail current $j_{\rm mtail}$ is represented in orange as it linked to the magnetospheric shape. Its description is similar to that of the magnetotail current of Fig. 2. Beside, two different perpendicular Alfvénic current loops ($j_{\rm alf}$) are represented on each side of the equatorial plane. The upper loops flow clockwise for an observer at the North-pole of the obstacle, while the Alfvén loops close to the center of the wake flows counter-clockwise. This current is described as an Alfvénic current due to the absence of any noticeable change in the density and the total magnetic field, as is it shown in the auxiliary material. The last current identified is a polarization current. It is visible in blue and noted $j_{\rm fast}$. This current flows around the two separated fast mode wings which are represented on each side of the wake via the blue semi-transparent cone-like layer. The fast mode wings represent the region in which the fast magnetosonic waves are propagating.

3.2.2. Intermediate situations at Alfvén Mach 2

In this section, an interaction regime with an upstream plasma velocity of $v_{\rm up} = 2v_{\rm A,0}$ (Alfvén Mach 2) is investigated. In this regime and between the cornerstones introduced in Section 3.1, we noticed two distinctive structures identified as the $+5{\rm E}3M_0\hat{z}|2v_{\rm A,0}$ and the $+40{\rm E}3M_0\hat{z}|2v_{\rm A,0}$ scenarios.

A schematic representation of the simulation results of the $+5e3M_0\hat{z}|2v_{\rm A,0}$ system is provided in Fig. 5. The magnetic moment magnitude is $M = 5\cdot10^3 M_0$ (see units in Table 1) and is oriented along $+\hat{z}$. We recall that the upstream field is antiparallel to $\hat{z}$ and the upstream plasma flows along $+\hat{x}$. The magnetic field at the surface in the equatorial plane is $B_{\rm surf} = 0.62B_0$ and the stand-off distance of this obstacle is $L_{\rm SO} = 0.84R_{\rm p}$. In this regime, we observed a typical C–F current ($j_{\rm C-F}$), represented in the dayside of the obstacle by means of orange arrows, and the shape of the magnetopause is represented by the orange semi-transparent layer. Its configuration is similar to that of the Lunar-Type: it flows dawnward in the equatorial plane and duskward in the terminator plane. The telluric current $j_{\rm tel}$ is plotted in yellow and flows clockwise in the equatorial plane seen from above. The bow-shock current $j_{\rm bs}$ is drawn with squared purple arrows while the shape of the bow-shock is displayed by the purple semi-transparent layer. As described in the earlier section, the C–F current, the bow-shock current and the telluric current are parallel at the subsolar point. On the tailside of the interaction region, we denoted a diamagnetic current, $j_{\rm slow}$, plotted in green here, in the equatorial plane in the wake of the obstacle. Its configuration is similar to the previously described slow-magnetonic mode current. A polarization current attached to the propagation of fast magnetosonic waves is also found again and represented here with blue arrows, while the spatial distribution of the fast magnetosonic mode polarization current is represented by the cone-like blue semi-transparent layer. Altogether, $j_{\rm slow}$ and the inner and outer parts of $j_{\rm fast}$ form a triangle shaped rings of current. Disturbances in the magnetic field without significant modification of the magnetic field magnitude and the density (see auxiliary material) are found. We described those disturbance by means of the Alfvénic current $j_{\rm alf}$ represented in red and showing two kinds of loops and their symmetric counterparts with respect to the equatorial plane. The outer current loops are clockwise for an observer at the North-pole of the obstacle, while the inner current loops are counter-clockwise.

The diagram of the $+40{\rm E}3M_0\hat{z}|2v_{\rm A,0}$ system obtained from simulation runs (see auxiliary materials) is shown in Fig. 6. The magnetic moment used in this case is $M = 40\cdot10^3 M_0$, leading to a surface magnetic field of $B_{\rm surf} = 5B_0$ and a stand-off distance $L_{\rm SO} = 1.68R_{\rm p}$ (parameters are summarized in Table 2). We distinguish again on the dayside the C–F current and the bow-shock current $j_{\rm bs}$ with the same properties as previously described. On the night side, are represented the slow magnetosonic diamagnetic current $j_{\rm slow}$, the fast magnetosonic mode polarization current $j_{\rm fast}$, the magnetotail current $j_{\rm mtail}$, and the secondary magnetotail current $j_{{\rm mtail}_2}$, similarly as Fig. 2.

3.2.3. Intermediate situations at Alfvén Mach 1

In the remainder of this section we present the diagrams for the scenarios using an upstream velocity $v_{\rm up} = 1v_{\rm A,0}$. The interaction regimes noticed between the cornerstones introduced in Section 3.1 are the $5{\rm E}3M_0\hat{z}|1v_{\rm A,0}$ and $+40{\rm E}3M_0\hat{z}|1v_{\rm A,0}$ systems. We briefly recall that the upstream plasma is flowing along $+\hat{x}$, the upstream magnetic field is oriented along $-\hat{z}$, and the planetary magnetic moment is directed along the $+\hat{z}$-axis.

The various currents appearing in the simulation of the $+5{\rm E}3M_0\hat{z}|1v_{\rm A,0}$ interaction type are summarized in Fig. 7a. This scenario employs a magnetic moment $M = 5\cdot10^3 M_0$, resulting in a surface field $B_{\rm surf} = 0.62B_0$, and a stand-off distance $L_{\rm SO} = 0.97R_{\rm p}$. An overview of the parameters is given in Table 2. A C–F current $j_{\rm C-F}$ is noticeable and plotted in orange. In this regime, we also observe the presence of a telluric current $j_{\rm tel}$ plotted in yellow, which flows clockwise in the equatorial plane viewed from above. A wake related diamagnetic current $j_{\rm slow}$ is present too and represented in green. Its dusk part flows sunward, while its dawn section flows anti-sunward. The current $j_{\rm slow}$ is visible in the center of the wake and flows antiparallel to $\hat{y}$. In this interaction system, Alfvén wings are fully formed and represented in Fig. 7a by the red semi-transparent tubes. The Alfvénic current $j_{\rm alf}$ related to the Alfvén wings is similar to that of Fig. 3: it is divided into components parallel and perpendicular to the local magnetic field (Neubauer, 1998). Consider first the component of the Alfvénic current parallel to the magnetic field, its dawn part flows toward the obstacle, while its dusk part flows in the opposite direction. Conversely, the northern and southern parts of the component of the Alfvénic current perpendicular to the field, flow anti-clockwise and clockwise, respectively, when seen by an observer at the North-pole of the obstacle.

The last scenario presented in this paper is the $+40{\rm E}3M_0\hat{z}|1v_{\rm A,0}$ system, which diagram is provided in Fig. 7b. The magnetic moment used in this interaction type is $M = 40\cdot10^3 M_0$, the surface magnetic field is therefore $B_{\rm surf} = 5B_0$ and the stand-off distance is $L_{\rm SO} = 1.94R_{\rm p}$. The C–F current $j_{\rm C-F}$ and the magnetotail current $j_{\rm mtail}$ are represented in orange, with the magnetopause as a semi-transparent orange layer. In this system, a diamagnetic slow magnetosonic wave related current $j_{\rm slow}$ is also present and drawn in green. The Alfvén wings are also clearly

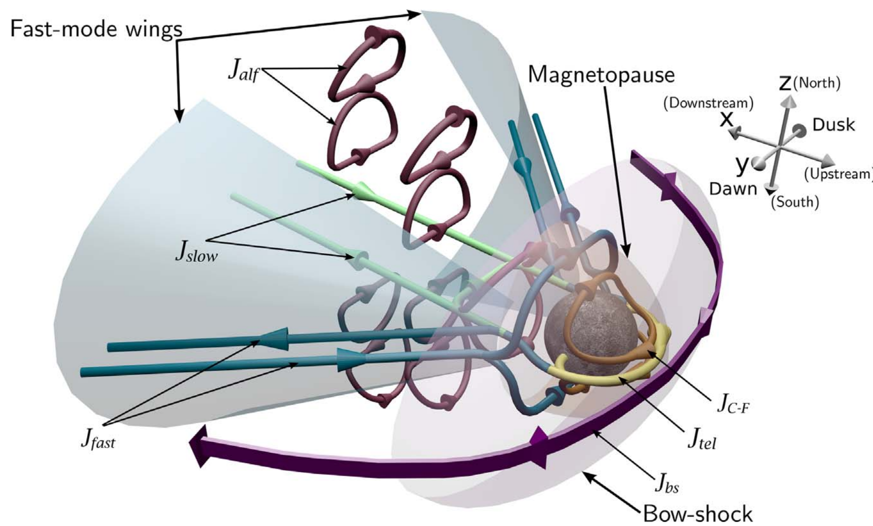

Fig. 5. Three-dimensional representation of the current structures for the $+5\text{E}3M_0\hat{z}|2v_{A,0}$ case (see Table 2 for parameters). Current description: same as Fig. 3. The upstream stellar wind velocity is $v_{up} = 2v_{A,0}$. (For interpretation of the references to color in this figure caption, the reader is referred to the web version of this paper.)

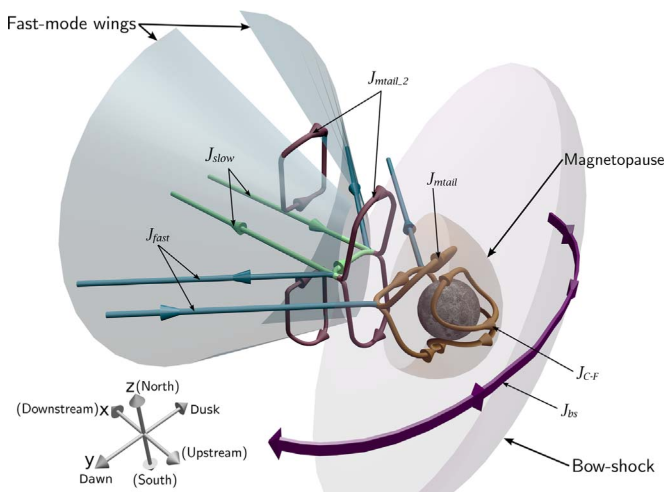

Fig. 6. Three-dimensional representation of the current structures for the $+40\text{E}3M_0\hat{z}|2v_{A,0}$ system (see Table 2 for parameters). Current description: same as Fig. 2. The upstream stellar wind velocity is $v_{up} = 2v_{A,0}$.

observed and represented here as tube-like semi-transparent red layers, with the corresponding j_{alf} plotted with red arrows.

4. Discussion

Our study is centered on the description of the configuration of the interaction region using the currents. We therefore focus on the various currents observed in the simulation results presented in the previous section. We organize this discussion using the stand-off distance detailed in Section 2. We first introduce the currents appearing at the earlier stage of the classification, and disappearing at the later stages. We start with the simplest cases, which correspond to scenarios where the stand-off distance is less than the planetary radius. A stand-off distance which is smaller than the planetary radius should be taken as an identifier of the interaction scenario. It is expected that a system showing a small stand-off distance presents the same properties as the inert obstacle system described in our previous study (Vernisse et al., 2013). Hence we discuss the telluric current j_{tel}, which is mostly noticeable in the case of inert and weakly magnetized obstacles (Figs. 4, 5, and Fig. 7a). Then we discuss the currents linked to the magnetosonic waves and the Alfvén waves, namely the diamagnetic currents j_{slow}, the fast mode polarization current j_{fast}, and the Alfvénic current j_{alf}. Those currents are observed around both inert obstacle and magnetized obstacles (Figs. 2–7). The next types of currents noticeable for larger stand-off distances are the Chapman–Ferraro (C–F) current j_{C-F}, the magnetotail current j_{mtail}, and the bow-shock current j_{bs}, which indicates the presence of discontinuities (Figs. 2–7). Ultimately, with the highest stand-off distances treated in this paper come fully developed magnetospheres and ring currents j_{ring} as well as the secondary magnetotail currents j_{mtail_2} (Figs. 2 and 3). An important point is the continuous and monotonic nature of every physical process mentioned in this section. All current magnitudes increase or decrease progressively as the parameters are changed.

4.1. Telluric current

The telluric current (identified in the results as j_{tel}) is due to the imperfect dielectric nature of the obstacle. Figs. 4, 5, and Fig. 7a show that the telluric current flows along the obstacle on the dayside. It is thus related to the Ohmic conductivity of the obstacle, and can simply be expressed using the electric field. The direction of the electric field in all configurations used in our study (the plasma flows along $+\hat{x}$, the upstream magnetic field is directed along $-\hat{z}$) is straightforwardly obtained from the frozen-in condition, which leads to an electric field directed antiparallel to $\hat{y}$. The telluric current flows parallel to the electric field inside the obstacle, and closes just above the surface of the obstacle. The magnitude of the telluric current is proportional to the magnetic Reynolds number of the planet $\mathcal{R}e$. This number is defined as the ratio between the convection velocity, i.e. the plasma velocity outside the obstacle, and the diffusion velocity inside the obstacle, which directly depends on the conductivity:

$$\mathcal{R}e = \frac{L_{char}\mu_0 v_{up}}{\eta}, \tag{4}$$

where L_{char} is the characteristic length of the obstacle, and η is the resistivity of the obstacle. The prime consequences is that for a dielectric obstacle, this current is only noticeable when the velocity of the plasma surrounding the obstacle is fast. This is the case for an inert obstacle embedded in a fast solar wind (e.g. the Earth moon), where the plasma surrounding the obstacle flows at a super-Alfvénic velocity. For strongly magnetized obstacles, the bow-shock and the magnetopause slow down the plasma before it reaches the obstacle. In this case the telluric current becomes negligible. Beside, in the configuration used in our study, the telluric current competes against the C–F current at the poles of the obstacle (in particular, Fig. 4), while

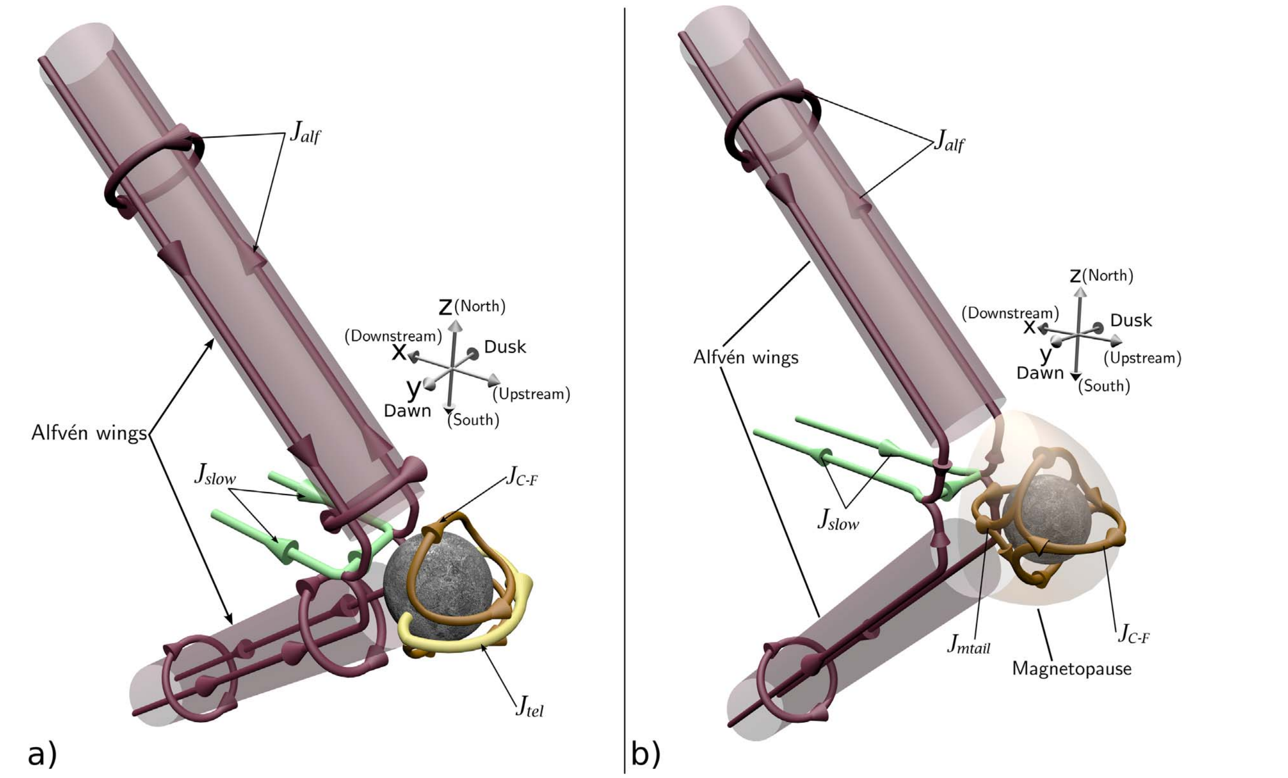

Fig. 7. Three-dimensional representations of the current structures of the (a) $5\mathrm{E}3M_0\hat{z}|1v_{A,0}$ and (b) $+40\mathrm{E}3M_0\hat{z}|1v_{A,0}$ systems (see Table 2 for simulation parameters). Description of the currents: same as Fig. 3, except for the red semi-transparent layer, which represents the Alfvén wings here. The stellar wind velocity is $v_{up} = 1v_{A,0}$. (For interpretation of the references to color in this figure caption, the reader is referred to the web version of this paper.)

they flow in the same direction in the equatorial plane. For planetary obstacle possessing a dipole field balancing the upstream plasma pressure, the C–F current becomes dominant and the telluric current, which magnitude depends on the diffusion velocity of the surrounding field into the obstacle, becomes negligible (see transition cases in Figs. 7a and b). It is known that at Mercury, the current induced by the conductivity of the obstacle play a role in closing the global magnetospheric current (Janhunen and Kallio, 2004; Jia et al., 2015). It is therefore consistent to simulate a non-perfectly dielectric obstacle and describe the closure of magnetospheric current system by telluric currents.

4.2. Slow magnetosonic, Alfvénic, and fast magnetosonic currents

The slow magnetosonic, fast magnetosonic, and Alfvénic currents are signatures of the propagation of the slow magnetosonic, fast magnetosonic, and Alfvén waves, respectively. Those waves are triggered by a perturbation in the plasma due to the obstacle itself and/or the magnetosphere. A plasma flowing around an obstacle, whether inert or not, creates a conic void region in the wake (Roussos et al., 2008). This region is replenished by diffusion through the void boundaries, creating pressure gradients at these locations. A diamagnetic current is shown to flow perpendicularly to both the local magnetic field and the pressure gradient (see Fig. 4). Specifically for a magnetic field along the $-\hat{z}$ direction, this process yields two distinct diamagnetic currents in the equatorial plane: sunward on the dusk side and anti-sunward on the dawn side. This observation holds for Lunar-Type obstacles and for all obstacles submitted to a slow upstream plasma and/or weak intrinsic field. In addition, one also observes a transwake diamagnetic current, which has its origin in the pressure gradient directed along $\hat{x}$ (Simon et al., 2012). The upstream plasma flows along $\hat{x}$, therefore the refilling of the wake induces a pressure gradient directed along the same direction. This generates a diamagnetic current flowing duskward in our results (Fig. 7a). In this paper, we focus on the evolution of the diamagnetic current through different regimes: we observe that the velocity of the upstream plasma together with the intrinsic planetary moment of the obstacle plays a major role in the disappearance of this current. The evolution is best shown in the $+5\mathrm{E}3M_0\hat{z}|2v_{A,0}$ and $+40\mathrm{E}3M_0\hat{z}|2v_{A,0}$ cases, in Figs. 5 and 6, respectively. Between those two scenarios, the diamagnetic current is pushed away from the obstacle as the magnetosphere develops, effectively acting as an obstacle. With higher upstream velocity regimes, the magnetosphere expands farther downstream due to frictions between the upstream plasma and the planetary field. Therefore the diamagnetic currents, which bound the void region created by the magnetosphere, are "pushed" further downstream.

We now examine the Alfvénic current. In this work, the Alfvénic current j_{alf} is primarily linked to the presence of Alfvén wings (Fig. 3). The orientation of the Alfvén wings is set by the bending of the local magnetic field. The Alfvénic current has two distinct components: (1) a circular current perpendicular to the local magnetic field, i.e. normal to the wing axes and (2) a current parallel to the local magnetic field, i.e. along the wings. For clarity, we represent the Alfvén wings as tubes attached to the poles of the obstacles, and oriented parallel to the local magnetic field (Figs. 3, 7a, and b). This description is accurate for interactions involving either a weakly magnetized obstacles (Fig. 7a) or sub-Alfvénic upstream plasma velocities (Fig. 3), or both (Fig. 7b). For super-Alfvénic plasma interactions involving a magnetized obstacle, the bow-shock becomes predominant and suppresses the Alfvén wings (Figs. 2, 4–6). For scenarios implying an inert obstacle, two main reasons explain the presence of Alfvén wings, and therefore Alfvénic currents. First, the conductivity of the obstacle, or more precisely, the magnetic Reynolds number of the planet. As introduced in Section 4.1, the finite conductivity of the obstacle generates a telluric current which flows inside the obstacle and closes in its surrounding plasma (Fig. 7a). The distortion of the field by this current pulls Alfvén wings at the northern and southern parts of the interaction region. This can be observed for Lunar-Type and Rhea-Type scenarios (Vernisse et al., 2013), as well as in the $+5\mathrm{E}3M_0\hat{z}|1v_{A,0}$ case (Fig. 7a). The second triggering effect is the refilling of the obstacle wake: as explained in the previous paragraph, a $-\hat{y}$-directed transwake current former due to pressure gradients is observed. This current distorts the magnetic field, and generates Alfvén wings, as shown by Simon et al. (2012). The configuration of the Alfvénic current is more complicated around moderately intermediate magnetized obstacles. Due to the particular field orientation investigated in this paper (southward upstream field and northward planetary moment), a double draping pattern appears in the nightside when increasing the magnetization strength of the obstacle. The superposition of the draping of the upstream magnetic field and the stretching of the planetary magnetic field lines leads to layered magnetic field lines alternatively towards and out of the obstacle. This pattern is particularly noticeable for the $+10\mathrm{E}3M_0\hat{z}|8v_{A,0}$ and the $+5\mathrm{E}3M_0\hat{z}|2v_{A,0}$ scenarios, depicted in Figs. 4 and 5, respectively. This field distortion in the nightside is partly due to the reconnection happening at the north and south poles of the obstacle, which accelerates the flow in these regions. When the bow-shock is fully developed (Fig. 2), the double draping pattern is no more noticeable.

In the remainder of this section, we consider the fast magnetosonic mode polarization current j_{fast}. This current is clearly noticeable in the outer boundary of the interaction region for weakly magnetized obstacles, and between the magnetopause and the bow shock for strongly magnetized obstacles (Figs. 2, 4–6). It is a signature of the propagation of fast magnetosonic waves. The absence of stationary solutions for fast waves at sub-Alfvénic regime (Neubauer, 1980) makes it to be impossible to observe in our simulation results for $v_{up} \leq 1v_{A,0}$. The fast mode polarization current has been described for the Lunar-Type scenario in our previous study (Vernisse et al., 2013), which details the evolution and disappearance at sub-Alfvénic velocities, and the related formulas to derive that current is provided in Section 2. An important point that need to be emphasized is the non-homogeneity of the propagation pattern of the fast waves. It propagates at $v_A + c_s$ in the equatorial plane and at v_A in the plane parallel to the magnetic field (following the typical Friedrich diagram, e.g. Kivelson and Russell, 1995). This last point implies that the fast magnetosonic mode polarization current is likely to merge with the Alfvénic current in the northern and southern parts of the interaction region. However, the fast waves current is distinguishable from the other magnetosonic waves in the equatorial plane. This is observed and noted for the Lunar-Type system (Vernisse et al., 2013). This observation still holds here for the $+80\mathrm{E}3M_0\hat{z}|8v_{A,0}$, $+10\mathrm{E}3M_0\hat{z}|8v_{A,0}$, $+5\mathrm{E}3M_0\hat{z}|2v_{A,0}$, and the $+40\mathrm{E}3M_0\hat{z}|2v_{A,0}$ scenarios in Figs. 2, 4, 5, and 6, respectively. To put it in a nutshell, two major points play an important role in the shape of the fast mode current: (1) the upstream plasma velocity and (2) the propagation of the fast waves along the $\hat{z}$-axis (i.e. the magnetic field). As for other magnetosonic waves, the fast wave propagation depends on the ratio between its propagation velocity and the plasma velocity. This explains the wings-like shape observed (Figs. 2, 4–6). In addition, the fast mode polarization current is concentrated in the equatorial plane for weakly magnetized obstacles, as shown in Vernisse et al. (2013). When increasing the planetary magnetization, the distribution of the current j_{fast} spreads away from the equatorial plane, as it is represented by the blue layers in Figs. 4–6. In the results of the $+80\mathrm{E}3M_0\hat{z}|8v_{A,0}$ situation (Mercury-Type), we observe the existence of the fast mode polarization current between the magnetotail and the bow-shock (Fig. 2). Observations of the transition between the $+10\mathrm{E}3M_0\hat{z}|8v_{A,0}$ and the $+80\mathrm{E}3M_0\hat{z}|8v_{A,0}$ reveal that the fast mode currents spread throughout the magnetosheath, but is particularly noticeable near the magnetopause.

4.3. Discontinuity currents: magnetopause and bow-shock

The bow-shock and the magnetopause are both identifiable via electromagnetic currents, namely the bow-shock current, the Chapman–Ferraro current, and the magnetotail current. These three currents are signatures of magnetic field, density, pressure, and velocity discontinuities in the interaction region.

The Chapman–Ferraro current is present in the dayside of the obstacle. Due to the range of planetary magnetic moment investigated in this work, the C–F current remains close to the obstacle, i.e. at a maximum distance of $2R_p$ ($\approx 10R_p$ for Earth, $\approx 1.5R_p$ for Mercury). The C–F current is observable when the planetary field at the surface is similar or stronger than the magnitude of the upstream magnetic field (Figs. 2–7). Therefore, the ratio surface magnetic field noted B_{surf} over the upstream field is a useful parameter to classify the interaction types, depending on the presence of the C–F current (see Table 2). As introduced in Section 2, the C–F current is a consequence of the compression of the planetary dipole field by the upstream plasma pressure. Thus, due to the northward orientation of the magnetic moment of the planet used in this work, the current j_{C-F} is directed westward in the equatorial plane and eastward in the terminator plane (Fig. 6). Although the spatial orientation of the Chapman–Ferraro current depends only on the planetary field, its magnitude depends on the pressure balance between the upstream plasma and the planetary field. A consequence of the orientation of the planetary field and the upstream field used in the results presented in this study is that the Chapman–Ferraro current, the bow-shock current, and the telluric current are all similar in the equatorial plane (see Fig. 4). It is therefore challenging to distinguish the contribution of each current in the output from the simulation. Future work using a different orientation could establish a clear distinction between the Chapman–Ferraro current and the bow-shock current. In order to describe the size of the magnetopause in this regime, it is important to take into account the upstream magnetic field pressure in the pressure balance in Eq. (1). Indeed, for an upstream velocity $v_{up} = 1v_{A,0}$ (Fig. 7b), the upstream dynamic pressure is equal to the upstream magnetic field pressure. In this case, only a weak friction force, which is proportional to the stellar wind velocity (Chodura and Schlueter, 1981), is exerted on the magnetosphere. This explains why the nightside of the interaction region is hardly developed. While the magnetopause is delimited on the dayside by the C–F current, the nightside interaction region is bounded by the magnetotail current. In our results and with the particular geometry used in this paper (northward intrinsic moment and southward IMF), the magnetotail current delimit the regions of trapped particles versus solar wind particles. This is due to the fact that in our simulation, reconnection occurs simultaneously at the north and south poles. A solar wind field line impinging the magnetosphere is draped. Once the IMF line “touches” the north and south poles of the obstacle, it reconnects. The draped part of the field line becomes attached to the planetary field, while a tailside field line of the planet becomes connected on both end to the IMF (see also supplementary material, Figures S1e, S2e, S3e, S4e, and S5e). In addition, we observed field lines connected on one end to the IMF and at the other end to the planetary field, but for a location limited at the surroundings of the poles. Thus, particles exchange between the magnetosphere and the solar wind is possible, but only for a brief moment. This configuration is very different to the well known dayside reconnection scenario, where field lines remain open while they are convected away across the whole interaction region. Also, in a scenario where the intrinsic planetary moment is tilted with respect to the incoming upstream velocity, a difference in convection time will appear between the magnetic poles. This means that due to the tilt angle, an IMF line will reconnect earlier at one pole compared to the other. Consequently, the field line remains open longer, enabling more particles to enter or escape the magnetosphere.

The second type of discontinuity current is the bow-shock current j_{bs}. The bow-shock is only present when the upstream velocity is greater than the fast magnetosonic wave group velocity. In our results, the bow-shock current flows westward in the planes perpendicular to $\hat{z}$. Conversely to the Chapman–Ferraro current which depends on the planetary moment orientation, the direction of the bow-shock current depends only on the orientation of the upstream field (Figs. 2, 4–6). Its magnitude depends on the balance between the planetary magnetic pressure and the upstream plasma pressure. The pressure balance is represented by the stand-off distance detailed in Section 2, Eq. (1), and provided for each scenarios investigated in this work in Table 2. The bow-shock current is a consequence of the deflection of plasma particles due to the local increase of the magnetic field. The fully developed shape of the bow-shock is represented by the semi-transparent purple layer in Figs. 2, 4–6. The important result concerning the bow-shock is that when the planetary magnetization is progressively increased, the bow-shock current first appears in the equatorial plane (perpendicular to the magnetic field) and further develops afterward along the z-axis (parallel to the magnetic field), as its own magnitude increases. This process is similar to the development of fast magnetosonic wings.

4.4. Ring, magnetosheath, and distant magnetotail currents

Other currents appear when the planetary body is highly magnetized, and when a developed magnetosphere dominates the interaction region. The first current that we observe when the magnetization of the obstacle is increased is the shocklet current identified in our results as j_{sho} (Fig. 2). The shocklet current is a precursor of the bow-shock current as explained by Bagdonat and Motschmann (2002b). However, this last study has been performed for a cometary obstacle, therefore the symmetry observed in our results is not reproduced in Bagdonat and Motschmann (2002b), due to the asymmetric property of mass-loading plasma effects. This current possesses the same properties as the bow-shock current. Therefore, it is first concentrated in the equatorial plane, and develops with magnetization strength along the magnetic field axis.

A small current, which is indicated as j_{ring} in Fig. 3, has been identified as following the pattern of a ring current. This current is a diamagnetic current due to the density depletion in the vicinity of the obstacle resulting from the shielding of the magnetosphere. Also, as explained earlier, the particular configuration of our simulation only allocate short reconnection window for particles to enter the magnetosphere. Thus, this leads to a pressure gradient directed radially outward the obstacle. Together with a northward dipole, this produces a diamagnetic current flowing in the equatorial plane, parallel to the Chapman–Ferraro current on the dayside and anti-parallel to the magnetotail current on the nightside. The ring current is only noticeable once a clear magnetosphere is built up, and the magnetopause stands at least one planetary radius away from the obstacle surface.

The last current investigated in this paper is a current that we name “secondary magnetotail current” j_{mtail_2}. This current is present because of the particular configuration of our interaction system. Its role is different from a typical magnetotail current, as it does not increase the planetary field in the lobes. This current is generated by the particular draping of the IMF (see auxiliary material), partly generated by the reconnection process as detailed earlier in this section. This current exists behind the limit of the nightside magnetosphere i.e. the shielded region, dominated by the planetary magnetic field. This current is only present at super-Alfvénic regime of interaction (e.g. Fig. 2) and absent in sub-Alfvénic cases (Figs. 3 and 7). We conclude that this current is due to a merging of the Alfvénic current and the fast magnetosonic current. At sub-Alfvénic regimes, only the Alfvénic wings are observable, while in super-Alfvénic, both types of waves are present, and a superposition of their interaction is likely to trigger a current having a similar pattern as the current j_{mtail_2}.

5. Conclusion

In this paper we expand upon the structures of currents described in our previous study (Vernisse et al., 2013). Starting from a Lunar-Type obstacle we implement a dipole magnetic moment in the core of the naked obstacle and observe the evolution of plasma structures depending on two parameters: the magnitude of the planetary magnetic moment and the upstream plasma velocity. We focus on a northward orientation of the magnetic moments with a southward IMF. First, we set the cornerstones in the parameter space, and then we develop the intermediate situations between the cornerstones. The transition from a Lunar-Type obstacle to a Mercury-Type obstacle shows that the Chapman–Ferraro current initially appears on the dayside of the obstacle. Even if the magnetosphere is not developed outside of the obstacle, the Chapman–Ferraro current flows on the surface in order to confine the magnetic field within the planet. The magnetotail current identified in the nightside region of the Lunar-Type obstacle is divided into two distinct loops due to reconnection processes happening at the southern and northern poles of the obstacle. This reconnection processes generate an acceleration of the plasma behind the reconnection region and causes a bending of the field lines downstream the wake. For stronger magnetic moments able to balance the stellar wind dynamic pressure, the bow-shock becomes detached. The deceleration of the flow around the obstacle (due to the existence of the bow-shock) decreases the impact of the reconnection process at the poles and therefore also decreases the twisting of the field lines in the wake. Also, the fast magnetosonic mode polarization current j_{fast} seen in the equatorial plane for super-Alfvénic simulations is translated downstream the wake due to the development of a shielded region in the vicinity of the obstacle. At this point we make an analogy with the case of the Lunar-type obstacle: while the perturbing object in the case of the Lunar-type is an inert obstacle, for the case of a developed magnetopause, one expects that the perturbing object is the region where the planetary magnetic field is dominant, also called the shielded region. When one looks at the transition regime between a Rhea-Type obstacle and a Ganymede-Type obstacle, we observe that, for upstream velocities $v_{\mathrm{up}} \geq 2v_{\mathrm{A},0}$ (or super-fast-magnetosonic), the general current configurations are similar. The differences lay in the ratio between the stellar wind velocity and the magnetosonic waves group velocity, which define how the plasma structures organizes in space. For upstream velocities $v_{\mathrm{up}} \leq 2v_{\mathrm{A},0}$ (or sub-fast-magnetosonic), we note the disappearance of the fast mode current, and therefore a structure centered on the Alfvén wings for weak magnetic fields. For a planetary dipole field stronger than the upstream magnetic field, we observe the development of a complete magnetosphere.

Acknowledgments

Yoann Vernisse acknowledged a Post-Doctoral fellowship at the International Max Planck Research School on Physical Processes in the Solar System and Beyond. The simulations were performed on the systems of the North-German Supercomputing Alliance.

The work by K.H.G. was financially supported by the Deutsches Zentrum für Luft- und Raumfahrt and the German Ministerium für Wirtschaft und Energie under contracts 50QW1101, 50OC1102, 50OW1501, 50QP1401, and 50 OC 1001.

The work of J.A.R. and U.M. is financially supported by the Collaboration Research Center 963, “Astrophysical Flow, Instabilities, and Turbulence” of the German Science Foundation.

Appendix A. Supplementary data

Supplementary data associated with this article can be found in the online version at http://dx.doi.org/10.1016/j.pss.2016.08.012.

References

Bagdonat, T., Motschmann, U., 2002a. 3D hybrid simulation code using curvilinear coordinates. J. Comput. Phys. 183, 470–485.

Bagdonat, T., Motschmann, U., 2002b. From a weak to a strong comet – 3D global hybrid simulation studies. Earth Moon Planets 90, 305–321.

Baumjohann, W., Treumann, R.A., 1996. Basic Space Plasma Physics. Imperial College Press, London, UK.

Boesswetter, A., Bagdonat, T., Motschmann, U., Sauer, K., 2004. Plasma boundaries at mars: a 3-d simulation study. Ann. Geophys. 22 (December), 4363–4379.

Boesswetter, A., Lammer, H., Kulikov, Y., Motschmann, U., Simon, S., 2010. Non-thermal water loss of the early Mars: 3D multi-ion hybrid simulations. Planet. Space Sci. 58

(December), 2031–2043.
Boesswetter, A., Simon, S., Bagdonat, T., Motschmann, U., Fränz, M., Roussos, E., Krupp, N., Woch, J., Schüle, J., Barabash, S., Lundin, R., 2007. Comparison of plasma data from ASPERA-3/Mars-Express with a 3-D hybrid simulation. Ann. Geophys. 25 (August), 1851–1864.
Borovsky, J.E., 2008. The rudiments of a theory of solar wind/magnetosphere coupling derived from first principles. J. Geophys. Res. (Space Phys.) 113 (August), A08228.
Case, N.A., Wild, J.A., 2013. The location of the Earth's magnetopause: a comparison of modeled position and in situ Cluster data. J. Geophys. Res. (Space Phys.) 118 (October), 6127–6135.
Chané, E., Saur, J., Neubauer, F.M., Raeder, J., Poedts, S., 2012. Observational evidence of Alfvén wings at the Earth. J. Geophys. Res. 117 (September), 9217.
Chodura, R., Schlueter, A., 1981. A 3D code for MHD equilibrium and stability. J. Comput. Phys. 41 (May), 68–88.
Durand-Manterola, H.J., 2009. Dipolar magnetic moment of the bodies of the solar system and the Hot Jupiters. Planet. Space Sci. 57 (October), 1405–1411.
Eastman, T.E., Frank, L.A., Peterson, W.K., Lennartsson, W., 1984. The plasma sheet boundary layer. J. Geophys. Res. 89 (March), 1553–1572.
Farrell, W.M., Desch, M.D., Zarka, P., 1999. On the possibility of coherent cyclotron emission from extrasolar planets. J. Geophys. Res. 104 (June), 14025–14032.
Fuselier, S.A., Trattner, K.J., Petrinec, S.M., 2000. Cusp observations of high- and low-latitude reconnection for northward interplanetary magnetic field. J. Geophys. Res. 105 (January), 253–266.
Ganushkina, N.Y., Liemohn, M.W., Dubyagin, S., Daglis, I.A., Dandouras, I., De Zeeuw, D.L., Ebihara, Y., Ilie, R., Katus, R., Kubyshkina, M., Milan, S.E., Ohtani, S., Ostgaard, N., Reistad, J.P., Tenfjord, P., Toffoletto, F., Zaharia, S., Amariutei, O., 2015. Defining and resolving current systems in geospace. Ann. Geophys. 33 (November), 1369–1402.
Gombosi, T.I., Dezeeuw, D.L., Groth, C.P.T., Powell, K.G., 2000. Magnetospheric configuration for Parker-spiral IMF conditions: results of A 3D AMR MHD simulation. Adv. Space Res. 26, 139–149.
Haaland, S., Gjerloev, J., 2013. On the relation between asymmetries in the ring current and magnetopause current. J. Geophys. Res. (Space Phys.) 118 (December), 7593–7604.
Janhunen, P., Kallio, E., 2004. Surface conductivity of Mercury provides current closure and may affect magnetospheric symmetry. Ann. Geophys. 22 (May), 1829–1837.
Jia, X., Slavin, J.A., Gombosi, T.I., Daldorff, L.K.S., Toth, G., Holst, B., 2015. Global MHD simulations of Mercury's magnetosphere with coupled planetary interior: induction effect of the planetary conducting core on the global interaction. J. Geophys. Res. (Space Phys.) 120 (June), 4763–4775.
Jia, X., Walker, R.J., Kivelson, M.G., Khurana, K.K., Linker, J.A., 2009. Properties of Ganymede's magnetosphere inferred from improved three-dimensional MHD simulations. J. Geophys. Res. (Space Phys.) 114 (September), A09209.
Kallio, E., Barabash, S., Janhunen, P., Jarvinen, R., 2008. Magnetized Mars: transformation of Earth-like magnetosphere to Venus-like induced magnetosphere. Planet. Space Sci. 56 (May), 823–827.
Kivelson, M.G., Bagenal, F. 2007. Planetary Magnetospheres, pp. 519–540.
Kivelson, M.G., Bagenal, F., Kurth, W.S., Neubauer, F.M., Paranicas, C., Saur, J., 2004. Magnetospheric interactions with satellites. In: Jupiter. The Planet, Satellites and Magnetosphere. Cambridge Planetary Science, Vol. 1. Cambridge University Press, Cambridge, UK, pp. 513–536.
Kivelson, M.G., Khurana, K.K., Russell, C.T., Walker, R.J., Warnecke, J., Coroniti, F.V., Polanskey, C., Southwood, D.J., Schubert, G., 1996. Discovery of Ganymede's magnetic field by the Galileo spacecraft. Nature 384 (December), 537–541.
Kivelson, M.G., Russell, C.T., 1995. Introduction to Space Physics. Cambridge University Press, Cambridge, UK, April.
Kriegel, H., Simon, S., Motschmann, U., Saur, J., Neubauer, F.M., Persoon, A.M., Dougherty, M.K., Gurnett, D.A., 2011. Influence of negatively charged plume grains on the structure of Enceladus' Alfvén wings: hybrid simulations versus Cassini Magnetometer data. J. Geophys. Res. 116 (October), 10223.
Kriegel, H., Simon, S., Müller, J., Motschmann, U., Saur, J., Glassmeier, K.-H., Dougherty, M.K., 2009. The plasma interaction of Enceladus: 3D hybrid simulations and comparison with Cassini MAG data. Planet. Space Sci. 57 (December), 2113–2122.
Lavraud, B., Larroque, E., Budnik, E., Génot, V., Borovsky, J.E., Dunlop, M.W., Foullon, C., Hasegawa, H., Jacquey, C., Nykyri, K., Ruffenach, A., Taylor, M.G.G.T., Dandouras, I., Rème, H., 2013. Asymmetry of magnetosheath flows and magnetopause shape during low Alfvén Mach number solar wind. J. Geophys. Res. (Space Phys.) 118 (March), 1089–1100.
Lavraud, B., Thomsen, M.F., Taylor, M.G.G.T., Wang, Y.L., Phan, T.D., Schwartz, S.J., Elphic, R.C., Fazakerley, A., RèMe, H., Balogh, A., 2005. Characteristics of the magnetosheath electron boundary layer under northward interplanetary magnetic field: implications for high-latitude reconnection. J. Geophys. Res. (Space Phys.) 110 (June), A06209.
Liemohn, M.W., Ganushkina, N.Y., Katus, R.M., de Zeeuw, D.L., Welling, D.T., 2013. The magnetospheric banana current. J. Geophys. Res. 118 (March), 1009–1021.
Marsch, E., 2006. Kinetic physics of the solar corona and solar wind. Living Rev. Sol. Phys. 3 (July).
Mauk, B.H., Zanetti, L.J., 1987. Magnetospheric electric fields and currents. Rev. Geophys. 25 (April), 541–554.
Mueller, J., 2011. A.I.K.E.F.: an adaptive hybrid model with application to fossil fields at Titan and Mercury's double magnetopause. (Ph.D. thesis). TU Braunschweig.
Mueller, J., Simon, S., Motschmann, U., Glassmeier, K.-H., Saur, J., Schüle, J., Pringle, G.J., 2010. Magnetic field fossilization and tail reconfiguration in Titan's plasma environment during a magnetopause passage: 3D adaptive hybrid code simulations. Planet. Space Sci. 58 (October), 1526–1546.
Mueller, J., Simon, S., Motschmann, U., Schüle, J., Glassmeier, K.-H., Pringle, G.J., 2011. A.I.K.E.F.: adaptive hybrid model for space plasma simulations. Comput. Phys. Commun. 182 (April), 946–966.
Mueller, J., Simon, S., Wang, Y.-C., Motschmann, U., Heyner, D., Schüle, J., Ip, W.-H., Kleindienst, G., Pringle, G.J., 2012. Origin of Mercury's double magnetopause: 3D hybrid simulation study with A.I.K.E.F. Icarus 218 (March), 666–687.
Neubauer, F.M., 1980. Nonlinear standing Alfven wave current system at Io – Theory. J. Geophys. Res. 85 (March), 1171–1178.
Neubauer, F.M., 1998. The sub-Alfvénic interaction of the Galilean satellites with the Jovian magnetosphere. J. Geophys. Res. 103 (September), 19843–19866.
Omidi, N., Blanco-Cano, X., Russell, C.T., Karimabadi, H., 2004. Dipolar magnetospheres and their characterization as a function of magnetic moment. Adv. Space Res. 33 (January), 1996–2003.
Omidi, N., Blanco-Cano, X., Russell, C.T., Karimabadi, H., Acuna, M., 2002. Hybrid simulations of solar wind interaction with magnetized asteroids: general characteristics. J. Geophys. Res. (Space Phys.) 107 (December), 1487.
Piddington, J.H., 1979. The closed model of the Earth's magnetosphere. J. Geophys. Res. 84 (January), 93–100.
Ridley, A.J., 2007. Alfvén wings at Earth's magnetosphere under strong interplanetary magnetic fields. Ann. Geophys. 25 (March), 533–542.
Roelof, E.C., Sibeck, D.G., 1993. Magnetopause shape as a bivariate function of interplanetary magnetic field B_z and solar wind dynamic pressure. J. Geophys. Res. 98 (December), 21.
Roussos, E., Müller, J., Simon, S., Bößwetter, A., Motschmann, U., Krupp, N., Fränz, M., Woch, J., Khurana, K.K., Dougherty, M.K., 2008. Plasma and fields in the wake of Rhea: 3-D hybrid simulation and comparison with Cassini data. Ann. Geophys. 26 (March), 619–637.
Saur, J., Grambusch, T., Duling, S., Neubauer, F.M., Simon, S., 2013. Magnetic energy fluxes in sub-Alfvénic planet star and moon planet interactions. Astron. Astrophys. 552 (April), A119.
Saur, J., Neubauer, F.M., Strobel, D.F., Summers, M.E., 1999. Three-dimensional plasma simulation of Io's interaction with the Io plasma torus: asymmetric plasma flow. J. Geophys. Res. 104 (November), 25105–25126.
Shue, J.-H., Chao, J.K., Fu, H.C., Russell, C.T., Song, P., Khurana, K.K., Singer, H.J., 1997. A new functional form to study the solar wind control of the magnetopause size and shape. J. Geophys. Res. 102 (May), 9497–9512.
Simon, S., 2015. An analytical model of sub-Alfvénic moon-plasma interactions with application to the hemisphere coupling effect. J. Geophys. Res. (Space Phys.) 120 (September), 7209–7227.
Simon, S., Bagdonat, T., Motschmann, U., Glassmeier, K.-H., 2006a. Plasma environment of magnetized asteroids: a 3-D hybrid simulation study. Ann. Geophys. 24 (March), 407–414.
Simon, S., Boesswetter, A., Bagdonat, T., Motschmann, U., Glassmeier, K.-H., 2006b. Plasma environment of Titan: a 3-D hybrid simulation study. Ann. Geophys. 24 (May), 1113–1135.
Simon, S., Kriegel, H., Saur, J., Wennmacher, A., Neubauer, F.M., Roussos, E., Motschmann, U., Dougherty, M.K., 2012. Analysis of Cassini magnetic field observations over the poles of Rhea. J. Geophys. Res. 117 (July), 7211.
Simon, S., Saur, J., Kriegel, H., Neubauer, F.M., Motschmann, U., Dougherty, M.K., 2011. Influence of negatively charged plume grains and hemisphere coupling currents on the structure of Enceladus' Alfvén wings: analytical modeling of Cassini magnetometer observations. J. Geophys. Res. (Space Phys.) 116 (April), A04221.
Simon, S., Saur, J., Neubauer, F.M., Motschmann, U., Dougherty, M.K., 2009. Plasma wake of Tethys: hybrid simulations versus Cassini MAG data. Geophys. Res. Lett. 36 (February), 4108.
Siscoe, G.L., Crooker, N.U., Erickson, G.M., Sonnerup, B.U.Ö., Siebert, K.D., Weimer, D.R., White, W.W., Maynard, N.C., 2000. Global Geometry of Magnetospheric Currents Inferred From MHD Simulations. Geophysical Monograph Series 118. American Geophysical Union, Washington, DC, p. 41.
Tsyganenko, N.A., Andreeva, V.A., 2015. A forecasting model of the magnetosphere driven by an optimal solar wind coupling function. J. Geophys. Res. (Space Phys.) 120 (October), 8401–8425.
Vernisse, Y., 2014. Classification of the interactions of planetary bodies with stellar winds by hybrid simulation. (Ph.D. thesis). TU Braunschweig.
Vernisse, Y., Kriegel, H., Wiehle, S., Motschmann, U., Glassmeier, K.-H., 2013. Stellar winds and planetary bodies simulations: lunar type interaction in super-Alfvénic and sub-Alfvénic flows. Planet. Space Sci. 84 (August), 37–47.
Wang, Y.-C., Mueller, J., Ip, W.-H., Motschmann, U., 2011. A 3D hybrid simulation study of the electromagnetic field distributions in the lunar wake. Icarus 216 (December), 415–425.
Wang, Y.-C., Mueller, J., Motschmann, U., Ip, W.-H., 2010. A hybrid simulation of Mercury's magnetosphere for the MESSENGER encounters in year 2008. Icarus 209 (September), 46–52.
Whang, Y.C., 1969. Field and plasma in the lunar wake. Phys. Rev. 186 (October), 143–150.
Wiehle, S., Plaschke, F., Motschmann, U., Glassmeier, K.-H., Auster, H.U., Angelopoulos, V., Mueller, J., Kriegel, H., Georgescu, E., Halekas, J., Sibeck, D.G., McFadden, J.P., 2011. First lunar wake passage of ARTEMIS: discrimination of wake effects and solar wind fluctuations by 3D hybrid simulations. Planet. Space Sci. 59 (June), 661–671.
Zarka, P., 2006. Plasma interactions of exoplanets with their parent stars and associated radio emissions. Ecole de Goutelas, vol. 28, pp. 191–242, March.